

Article

Transferring Crystallization Conditions from Small to Larger Scale for Achieving Targeted Crystal Morphologies of an Active Pharmaceutical Ingredient

Nicolás Antonio Ramos Ojeda  and Matthias Kind * 

Institute for Thermal Process Engineering, Karlsruhe Institute of Technology, Kaiserstraße 12, 76131 Karlsruhe, Germany; nicolas.ramos@kit.edu

* Correspondence: matthias.kind@kit.edu

Abstract: Crystal morphology plays a critical role in the processability and physicochemical behavior of active pharmaceutical ingredients. Manipulating crystal morphology involves consideration of crystallization conditions such as temperature, supersaturation, and solvent choice. Typically, experimental screenings on a small scale are conducted to find targeted crystal morphologies. However, results from such small-scale experiments do not assure direct success at a larger scale, particularly if the small-scale setup differs significantly from a conventional stirred crystallizer. In this study, we successfully validated the morphologies observed in the small-scale experiments of an exemplary API, Bitopertin, when scaled up by a factor of 200, through the maintenance of identical process conditions and geometrical vessel relations. This successful scalability highlights the significant potential of small-scale crystallization studies to provide a reliable foundation for further exploration in large-scale endeavors.

Keywords: active pharmaceutical ingredients; crystal morphology; scale-up; evaporative crystallization; Bitopertin



Citation: Ramos Ojeda, N.A.; Kind, M. Transferring Crystallization Conditions from Small to Larger Scale for Achieving Targeted Crystal Morphologies of an Active Pharmaceutical Ingredient. *Crystals* **2024**, *14*, 42. <https://doi.org/10.3390/cryst14010042>

Academic Editor: Tom Leyssens

Received: 6 December 2023

Revised: 22 December 2023

Accepted: 26 December 2023

Published: 28 December 2023



Copyright: © 2023 by the authors. Licensee MDPI, Basel, Switzerland. This article is an open access article distributed under the terms and conditions of the Creative Commons Attribution (CC BY) license (<https://creativecommons.org/licenses/by/4.0/>).

1. Introduction

Crystal morphology, referring to the external shape of a crystal, holds immense significance when determining the processability, physicochemical and therapeutical behavior of active pharmaceutical ingredients (APIs) [1–3]. For instance, equant-shaped morphologies, also known as isometric morphologies, can enhance the flowability and compressibility of API particles [4,5], making them more suitable for tablet formulation and other manufacturing processes [6–8]. Furthermore, crystal morphology also influences the dissolution profiles of APIs, ultimately impacting their therapeutic efficacy [9–13]. As can be inferred from the above, there is a preference for the attainment of equant-shaped crystals [3,14,15]. In contrast, needle-like crystals are generally undesirable [16,17].

The crystal morphology is evidently subjected to the crystal form [3,18], also termed polymorph or crystal structure. As a result, substantial changes in crystal morphology can occur by altering the underlying crystal form. Nevertheless, it is generally more advantageous to manipulate the morphology while preserving the stable crystal form. This avoids potential challenges linked to the metastability of a new crystal form, which in turn might change during further processing or storage, resulting in different product properties. In striving to achieve a desired crystal morphology, intentional manipulation of various factors becomes necessary, including precise temperature control, careful adjustment of supersaturation levels, and thoughtful selection of solvents, among other things. Temperature plays a critical role in regulating crystal growth and nucleation rates, as different temperatures can promote specific crystal habits [11,19,20] or alter the kinetic pathways of crystal formation, as postulated in earlier literature [18,21] and revisited in more recent contributions [22–24]. Supersaturation, on the other hand, can affect the growth rates along

different crystal faces [25–29]. Additionally, the choice of solvent influences the interactions with solute molecules [30–33], thereby influencing the resulting morphological characteristics, as evidenced in several APIs [34–38]. By understanding and precisely manipulating these factors, alternatives for control over the crystal morphology of APIs can be achieved in order to obtain desired morphologies and secure the performance of the final drug product.

Due to the limited availability of the active pharmaceutical ingredient (API) in the development stage, conducting comprehensive experiments on a large scale is impractical [14,39]. As a result, experimental screenings on a small scale are of more interest when exploring various process conditions [40,41] and identify those that lead to the desired crystal morphologies. Once optimal process parameters are determined on a small scale, they have to be translated and applied to larger-scale production [42–45]. Thus, small-scale experimental screenings serve as crucial initial steps in the development of crystallization processes, providing valuable insights and guiding the design of larger-scale production methods for APIs. It is important to note that, although small-scale experiments are valuable for optimizing process conditions and achieving desired crystal morphologies, direct scaling up to larger production volumes has not always been successful [14,46,47]. This was especially true when there are significant differences between the small-scale setup and the conventional stirred crystallizers commonly used in industrial processes. These differences can affect the mixing dynamics, which in turn have an impact on the resulting crystal morphology [14,40,47–50]. Therefore, careful consideration and adjustments are necessary when transitioning from small-scale to large-scale production to ensure desired outcomes.

Within this context, various small APIs ($MW \approx 500 \text{ g mol}^{-1}$) from Fa. Hoffmann La-Roche (Bitopertin, Balapiravir Hydrochloride, DPP-IV Inhibitor) were examined in a previous study [51]. The objective was to improve their morphology from needle-like to isometric crystals, for the reasons outlined above. The selection of these APIs was based on their degree of equivalence to other APIs and their accessibility for research purposes. Consistent with the aforementioned considerations, the morphological screening adheres to the traditional progression from small to large scales. The primary aim of this study is to verify the transferability of results derived from a miniaturized crystallizer to larger scales, which hold significant economic interest in production.

In particular, the morphological screening in small scale employed an advanced and commonly available commercial miniaturized 5 mL crystallization system (Crystalline, Technobis). This system closely resembles the geometry and mixing conditions of larger crystallizers, making it a suitable platform for the experiments, in accordance with the scale-up considerations mentioned above. The authors of this contribution developed an augmented version of this system that allows controlled evaporative crystallization. By independently adjusting factors such as temperature, supersaturation buildup (evaporation rate), and solvent selection, specific process conditions were identified that consistently produced more equant-shaped morphologies while maintaining the stable crystal form.

As previously underscored, these results necessitate validation on a larger scale. What is more interesting is the fact that, to the authors knowledge, there are currently no experimental data available that verify the results in terms of morphology obtained from this highly miniaturized evaporative crystallization system when applied to larger crystallizers. Therefore, the purpose of this study is also to address the lack of experimental data and investigate the transferability of the obtained crystal morphologies from the miniaturized device to a larger intermediate scale. By doing so, this contribution aims to provide valuable insights into the scalability and applicability of the obtained morphologies in a larger production setting.

The upscaling process is to be tested in a liter-scale crystallizer, which represents a significant 200 fold increase in scale compared with the miniaturized crystallizers used in the cited study [51]. From the mentioned APIs, Bitopertin, Form A has been singled out for its wide spectrum of observed morphologies. This makes it an ideal candidate to test whether these morphologies can be observed in large scales, aiming not only to achieve the desired isometric morphology but also needle-like forms. The objective

is to prove the scalability of any aimed morphology. In order to achieve comparable crystal morphologies to those obtained in the small-scale experiments, the emphasis of this contribution is placed on meticulously replicating the exact process conditions, including the supersaturation profile, temperature, and solvent used in the miniaturized device. It is hypothesized that, by maintaining fidelity to the process conditions employed in the small-scale experiments, the likelihood of obtaining similar crystal morphologies can be increased. While the primary focus is on the transferability of crystallization across scales, this work also includes a morphology assessment post solid–liquid separation. This step aims to identify any disparities between findings obtained during crystallization and those observed afterward and is undertaken because ensuring the preservation of crystal quality through the separation and drying stages is crucial for standard evaluation.

While it is undeniable that mixing dynamics play a crucial role in determining crystal morphology, a more comprehensive comparison becomes particularly crucial when transitioning from an intermediate liter-scale stage to a pilot or industrial environment. Therefore, in this study focusing on the upscaling from milliliter to liter scale, an approximate approach was adopted. This approach considered factors such as geometry similarity and constant stirrer tip speed. The objective is to achieve a comparable level of mixing and suspension in both scales.

2. Materials and Methods

2.1. Bitopertin

Bitopertin is a glycine transporter type 1 inhibitor, and among its four distinct crystal forms, polymorph A is the stable form [52]. This stable polymorph serves as the raw material for our research and is also the desired polymorph for our crystallization experiments, so as to ensure that any morphological changes are not related to the production of an undesired metastable polymorph. We obtained Bitopertin from F. Hoffmann-La Roche (purity > 99.9%), who developed the substance and kindly supplied it for our studies. Under a wide range of crystallization temperatures, supersaturation ratio and in several solvents, Bitopertin Form A crystallizes predominantly in a needle-like crystal morphology, as depicted in Figure 1. This morphology is inherently undesirable, as outlined in the introduction. Nevertheless, our previous studies on this API, conducted at the miniaturized scale, successfully identified specific process conditions that enable the production of isometric crystals using controlled evaporative crystallization [51].

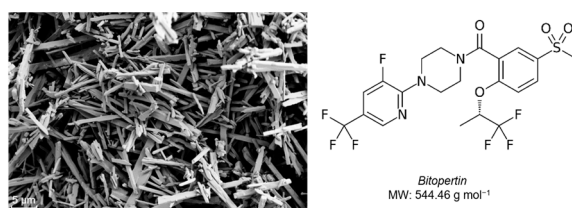


Figure 1. Crystal morphology and chemical structure of Bitopertin.

This current study revisits these process conditions and observed crystal morphologies to delineate the starting points from the miniaturized scale to be validated in the large scale.

2.2. Miniaturized Crystallizer (ml Scale)

The thorough morphological screening of Bitopertin was conducted in a miniaturized scale, hereinafter abbreviated as ml scale. These experiments utilized the already mentioned system Crystalline, which was augmented specifically for controlled evaporative crystallization as illustrated in Figure 2.

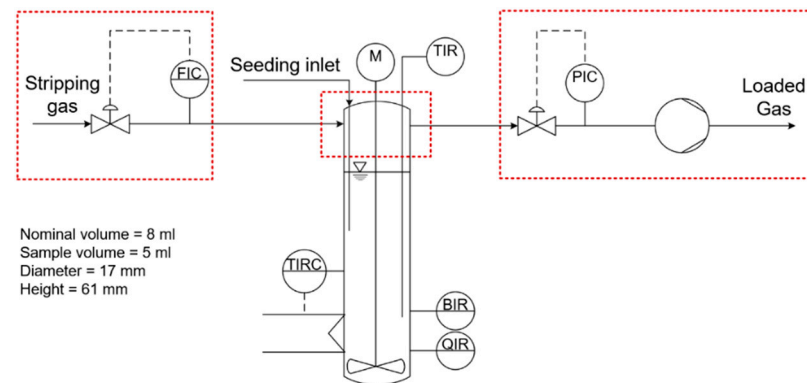


Figure 2. Experimental setup of the ml scale crystallizator (Crystalline) augmented for controlled evaporative crystallization as illustrated in [51]. The red delimited areas illustrate the modifications from the standard setup for controllable evaporative crystallization.

The temperature at the crystallizator walls was controlled by the integrated controller of the device (TIRC). The mixing of the suspension was accomplished using a pitched four-blade stirrer, attached to the magnetic coupling in the glass reactor lid. The stirring speed was set at 1000 RPM. The transmissivity was measured across the reactor (QIR) and the inline monitoring of the crystal morphology was facilitated by internal CCD cameras (BIR). Images with a resolution of $2.8 \mu\text{m}/\text{pixel}$ and size of 480×640 pixels were taken every 10 s.

The controlled still evaporation (no bubbles) was achieved by means of a stripping gas (nitrogen) introduced into the vial and passed over the liquid surface to promote evaporation. To regulate the pressure, a vacuum pump (LVS 105 T—10 ef, Welch Co., Ilmenau, Germany) is connected to the respective vacuum controller (Vacuu-Select controller, Vacuubrand Co., PIC, Wertheim, Germany) for each reactor. Thermal mass flow meter controllers (EL-Flow-Select, Bronkhorst Co., FIC, Ruurlo, The Netherlands) were installed in each reactor to precisely adjust the stripping gas flow within a fine range of 0.005–0.500 mL/min. Customized lids, provided by Technobis, were equipped with four openings to serve as gas and vapor inlets and outlets, ports for introducing seed crystals, and openings for inserting temperature sensors (TIR) into the vials.

2.3. Large Crystallizator (l Scale)

To validate the transferability of promising process conditions from the ml scale experiments to a larger scale, hereinafter referred as l scale, we performed experiments using the experimental setup depicted in Figure 3. The l scale setup closely resembled the ml scale crystallizator but had a usable volume 200 times larger.

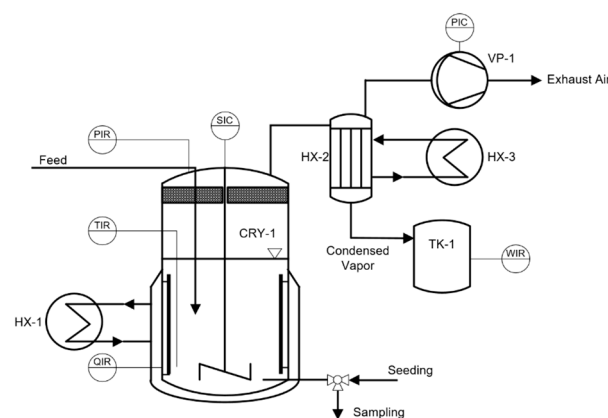


Figure 3. Experimental setup of the l scale crystallizator for controlled evaporative crystallization.

The 1 scale crystallizator (CRY-1) utilized in this setup was a double-wall glass vessel with four baffles, 11 cm internal diameter, and a maximum volume of 1.5 L. As shown in Figure 3, a demister at the top prevents droplet entrainment during evaporation. For proper suspension mixing, a 3 bladed propeller stirrer (IKA, shaft length: 350 mm, stirrer diameter: 45 mm, shaft diameter: 8 mm, Staufen, Germany) controlled by a motor (SIC, RZR 2102, Heidolph electronic stirrer controller, Kelheim, Germany) is equipped in the crystallizator. System pressure and boiling temperature were regulated by the vacuum pump integrated controller (VP-1, CVC-2, Vacuumbrand, Wertheim, Germany). A thermostat (HX-I, ECO Gold RE 1050, Lauda, Lauda-Königshofen, Germany) controls the circulation of a service stream along the crystallizator jacket, defining the solution temperature and evaporation rate. The vapor generated in the crystallizator was condensed in the condenser (HX-2) utilizing a water–ethylene glycol mixture as the cold service, which was regulated by a second thermostat (HX-3, ECO Gold RE 630, Lauda, Lauda-Königshofen, Germany). The condensed vapor was collected in a glass bottle (TK-1) placed on a balance (WIR, CPA5201, Sartorius, Göttingen, Germany) for weighing.

The measuring technique in the crystallizator CRY-1 includes a PT-100 temperature sensor (TIR), a pressure sensor (PIR), and a turbidity sensor (QIR) from Mettler Toledo model FSC402 (Gießen, Germany), capable of detecting the onset of nucleation. The data of these sensors and the previous indicated controllers were recorded through a user interface programmed in LabView (National Instruments, Austin, TX, USA). Sampling and seeding were facilitated by a three-way valve connected to a stainless-steel cannula (inner diameter: 1.9 mm) mounted on the crystallizator. To prevent internal crystallization, the cannula was placed in a heated aluminum block.

2.4. Resemblance between Scales

In order to achieve geometric resemblance between the 1 scale and ml scale crystallizators, careful consideration was given to the selection of system dimensions, both systems and a schematic representation of key dimensions for geometrical comparison are illustrated in Figure 4.

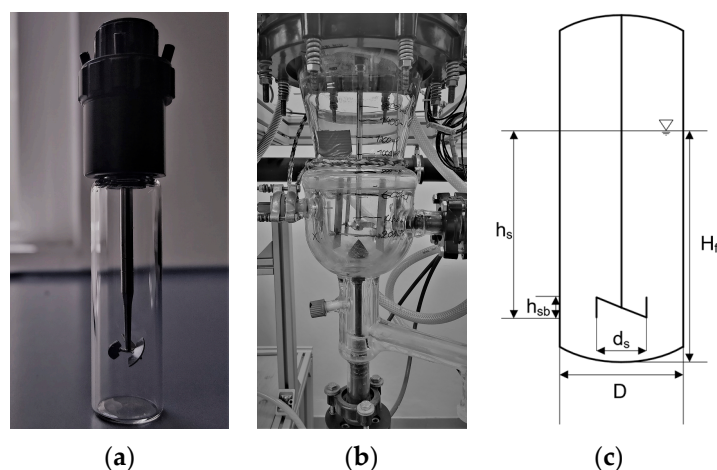


Figure 4. Employed crystallizators (a) ml scale and (b) 1 scale. (c) Schematic representation of key dimensions for geometrical comparison.

The 1 scale system was chosen to closely match the typical dimension ratios observed in the ml crystallizator, including the diameter of the crystallizator (D) in relation to the diameter of the stirrer (d_s), the level height (H_f) in relation to the height of the stirrer (h_s), and the level height in relation to the diameter of the crystallizator. A comprehensive comparison of these dimensions can be found in Table 1, which highlights the similarities between the two crystallizators. Additionally, the selected stirrer in the 1 scale shares several characteristics with the stirrer used in the ml scale, such as the type of stirrer, the number

of blades (n_s), and the angle. However, one noticeable difference between the two systems is the presence of four baffles in the l scale setup, which are not utilized in the ml scale. Overall, from a constructional standpoint, the l scale crystallizator closely resembles the characteristics of the ml scale crystallizators, ensuring a substantial similarity between the two systems.

Table 1. Key dimensions and characteristics of the crystallizators.

Parameters		Units	ml Scale	l Scale
Construction material	-	-	Glass	Glass
Filling Volume	V	mL	5	1200
Impeller type	-	-	Bladed propeller	Bladed propeller
Number of blades	n_b	-	3	3
Stirrer speed	n	min^{-1}	1000	178
Impeller tip speed	n_t	m s^{-1}	0.42	0.42
Stirrer diameter	d_s	mm	8	45
Crystallizator diameter	D	mm	15	110
Liquid coverage of the stirrer	h_s	mm	14	75
Stirrer blade height	h_{sb}	mm	11	5
Level height	H_f	mm	24.3	125
Blade inclination to the horizontal	α	$^\circ$	60	45
Number of baffles	n_b	-	0	4
Height ratio	H_f/h_s	-	1.7	1.7
Diameter ratio	d_s/D	-	0.5	0.5
Height-to-diameter ratio	H_f/D	-	1.5	1.6

In terms of operational considerations, there are various scale-up rules that address different mixing needs in the context of crystallization. Three commonly used scale-up rules for stirrer speed are: equivalent input energy per unit volume, similar maximum dissipation energy, and equivalent tip speed of the impeller [48–50,53–55]. In this study, equivalent stirrer tip speed was the chosen criterion to determine the number of agitations per minute in the l scale crystallizator. In the ml scale, a speed of 1000 min^{-1} was used, whose equivalent speed was 178 min^{-1} in the l scale crystallizator to fulfil the criterion.

2.5. Evaporative Crystallization

In both experimental setups, the execution of the experiments follows the same procedure. Prior to evaporation, feed solutions with defined supersaturation, based on the intended crystallization temperature, were prepared. We followed the solubility curves of Bitopertin, as given in [51]. The solutions were heated to the dissolution temperature (T_d), which was maintained for 1 h to ensure complete dissolution of all solid Bitopertin. The dissolution temperature intentionally exceeded the solubility temperature (T^*) by $5 \text{ }^\circ\text{C}$. Subsequently, the clear solution underwent rapid cooling to achieve the targeted crystallization temperature (T_c), with the cooling process conducted swiftly to prevent crystal formation during this step.

The supersaturation buildup trajectory was set to be equal in both small and large scales by setting the same time to evaporate half of the solvent τ_{50} at given T_c . Figure 5 illustrates two representative courses of the nominal supersaturation ratio as a function of the time to evaporate half of the solvent. One case corresponds to a τ_{50} value of 60 min, while the other case has a τ_{50} value of 210 min.

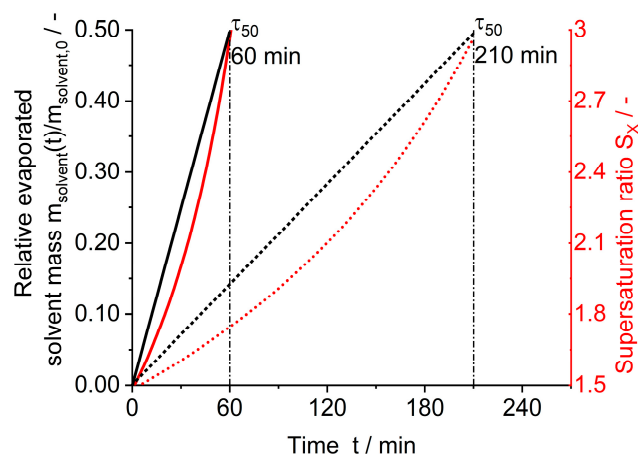


Figure 5. Exemplary supersaturation course (depicted in red) as function of the time to evaporate the half of the solvent ($\tau_{50} = 60$ and 210 min) at a constant temperature and pressure. The corresponding relative mass of evaporated solvent is plotted on black.

The supersaturation ratio is determined using Equations (1) and (2). Equation (1) describes the supersaturation buildup until nucleation occurs. During the evaporation phase, the amount of evaporated solvent in the solution depends on the evaporation rate, \dot{m}_v , as described in Equation (3). In the miniaturized scale, this rate is influenced by the volumetric flow of the stripping gas, \dot{V}_{in,N_2} , pressure p , temperature T , and the specific solvent, as outlined in Equation (4). The coefficients a and b in Equation (4) are determined through calibration experiments prior to the crystallization experiments.

$$S_X(t) = \frac{X_{API}(t)}{X_{API}^*(T_c)} \quad (1)$$

$$X_{API}(t) = \frac{m_{API}(t=0)}{m_{solvent}(t)} \quad (2)$$

$$m_{solvent}(t) = m_{solvent,0} - \int_0^t \dot{m}_v(t) dt \quad (3)$$

$$\dot{m}_v = f(\dot{V}_{in,N_2}) = a \cdot \dot{V}_{in,N_2}^b \quad (4)$$

At the larger scale, the evaporation occurred at boiling conditions, determined by the set vacuum pressure. Thus, there was no need for stripping gas to remove the solvent. Instead, the evaporation rate was regulated by the heat flow generated from the temperature difference between the fluid in the crystallizator jacket and the solution. Established methods and correlations were utilized to determine the jacket temperature necessary to achieve the desired evaporation rate [56]. The real evaporation rate over time is determined thanks to the inline-weighting of the condensed mass.

In the case of seeded experiments, the injection of seed material took place once T_c was reached and shortly before the start of evaporation. The seed material was prepared as suspension of the powdered raw material in a slightly supersaturated solution (with a supersaturation ratio $S_x = 1.1$) at a temperature of 20 °C. The solid fraction in the seeding suspension remained constant across experiments, typically at 1 wt%. The median crystal dimensions measure 5.17 μm in length and 3.47 μm in width. Prior to use, the suspension was thoroughly mixed for at least 1 h at a speed of 700 RPM. In the ml scale, 50 μL of the seeding suspension was injected into the solution. At the liter scale, 5 mL were injected into the solution.

2.6. Crystal Morphology and Structure Analysis

The morphology analysis relies on microscopic assessment of crystals during and after crystallization. In the ml scale, the crystallization can be visualized inline. However, the morphology analysis is performed offline based on the acquired images. For the l scale, there are not cameras integrated in the setup. Therefore, in order to evaluate the morphology of the crystal during the crystallization under the same optic, samples were taken from the large crystallizer and dispersed in vials with saturated solutions, which were put in the cells of Crystalline, while acquiring images.

The morphology was quantified using the aspect ratio, AR , calculated as the quotient between the major axis, x_{\max} , and minor axis, x_{\min} of the elliptical contour around the detected crystal. The characterization of the crystal morphology is based on the median value of the AR . The evaluation of x_{\max} and x_{\min} also enables the assessment of the crystal size distribution (CSD) along these two dimensions.

From both scales, the resulting product suspensions were subjected to solid–liquid separation. This involved filtration and drying under the crystallization temperature. From the dry material, the crystal structure is examined using powder X-ray diffraction (XRPD), and an additional morphology assessment is conducted to discern potential disparities between the findings obtained during the crystallization process and those observed post-crystallization.

3. Results

3.1. Miniaturized Crystallizer (ml Scale)

The extensive experimentation conducted at the ml scale and comprehensively discussed in [51] allowed us to explore a wide range of combinations while utilizing minimal material. Thereby we could identify the most favorable trends for the crystallization of isometric crystals and also the operation conditions that tend to promote acicular crystals.

In particular, three solvents—ethanol, 1-propanol, and 2-propanol—were investigated. These solvents were chosen based on their compliance with Q3C guidelines for residual solvents, ensuring a hazard-free level. Additionally, their solubility behavior with the API was considered, with ranges defined as soluble (30–10 mL solvent/g API) or sparingly soluble (100–30 mL solvent/g API) according to the European Pharmacopeia [57]. Various experimental conditions were explored, encompassing the crystallization temperature T_c , supersaturation buildup indicated by the evaporation time to evaporate the half of the solvent τ_{50} , and the presence or absence of seeding crystals. Table 2 summarizes qualitatively the observed morphologies based on the aforementioned variables.

Specifically, we found that, in the case of ethanol as a solvent, spontaneous crystallization of isometric crystals is possible when the supersaturation is smoothly built up, but only at higher temperatures of 45 and 55 °C. Additionally, the use of seed material in ethanolic solutions proved to be an effective strategy for obtaining more isometric crystals, regardless of whether the evaporation was conducted rapidly or slowly. On the other hand, irrespective of the solvent used, spontaneous nucleation and rapid evaporation consistently resulted in an acicular crystal morphology in all of the cases performed under these two conditions.

As previously stated, our primary objective is to successfully transfer process conditions in order to achieve desired crystal morphologies, with a specific emphasis on isometric and needle-like crystals, when operating at a larger l scale. We identified three distinct sets of process conditions from Table 2 for this purpose, designated as Cases I, II, and III. In the subsequent sections, we will thoroughly examine the outcomes of these cases.

Case I involves the crystallization of Bitopertin in ethanol without the use of seeding, employing slow evaporation ($\tau_{50} = 210$ min) at a crystallization temperature of 45 °C. The resulting crystals exhibit a distinct isometric morphology, which we expect to be observed when scaling up the process. Numerous replicates of the experiment have also consistently yielded a highly isometric morphology, demonstrating a noteworthy level of reproducibility despite the occurrence of spontaneous nucleation.

Table 2. Overview of the observed crystal morphology of Bitopertin obtained by evaporative crystallization in the ml scale. The process conditions to be validated in the l scale are highlighted in gray and named henceforth as Case I–III.

Ethanol					
		without seeding		with seeding	
T_c	τ_{50}	60 min	210 min	60 min	210 min
15 °C		needle, rod-like	needle, rod-like	isometric, rod-like	isometric, rod-like
30 °C		Case III needle, rod-like	needle, rod-like	isometric	isometric
45 °C		needle, rod-like	Case I isometric	isometric	Case II isometric
55 °C		needle, rod-like	isometric	-	-
1-propanol					
		without seeding		with seeding	
T_c	τ_{50}	60 min	210 min	60 min	210 min
15 °C		-	needle	needle	needle
30 °C		needle	needle	-	needle, rod-like
45 °C		needle	needle	isometric, rod-like	isometric, rod-like
55 °C		-	needle		
2-propanol					
		without seeding		with seeding	
T_c	τ_{50}	60 min	210 min	60 min	210 min
15 °C		needle	needle	needle	needle
30 °C		needle	needle	-	-
45 °C		needle	needle	needle	isometric, rod-like
55 °C		gel	needle	-	gel

Continuing with Case II, the crystallization process was carried out in ethanol at 45 °C, similar to Case I. However, in this case, seed material was introduced. Once more, isometric crystals were obtained under these conditions. In this case, the use of seed material provides an opportunity for a more controlled crystallization process, which is of significant interest in large-scale endeavors, which are mainly performed with seeding. Furthermore, based on the results exhibited in Table 2, even if the process execution deviates slightly from the set temperature or if the evaporation rate is faster or slower than the desired level, crystallization is still expected to occur within an operational window that favors the formation of isometric crystals.

Lastly, in Case III, the implemented process conditions yielded the formation of needle-like crystals. This case specifically utilizes ethanol as the solvent, excludes the use of seeding, and has a crystallization temperature of 30 °C, with a rapid evaporation process. Although the morphology of needle-like crystals may not align with the preferences in pharmaceutical crystallization, it presents an opportunity to verify the effectiveness of the process conditions to obtain a determined morphology. Validating this case in the l scale should present less challenges than the other cases. This is indicated by the results presented in Table 2, where it is evident that the needle morphology is the most common morphology for this API.

The morphologies of the crystals obtained in each selected case are visually depicted in Figure 6. While these morphologies can be observed in real time (inline camera), it is crucial to ensure their preservation through the solid–liquid separation and after drying,

which serves as the standard procedure when evaluating the quality of the crystals. To address this, we have captured and evaluated microscopic images of the dry product. The careful and meticulous procedure followed during the solid–liquid separation contributes to a satisfactory qualitative agreement between the morphologies observed in real time and those observed offline after drying, as demonstrated in Figure 6.

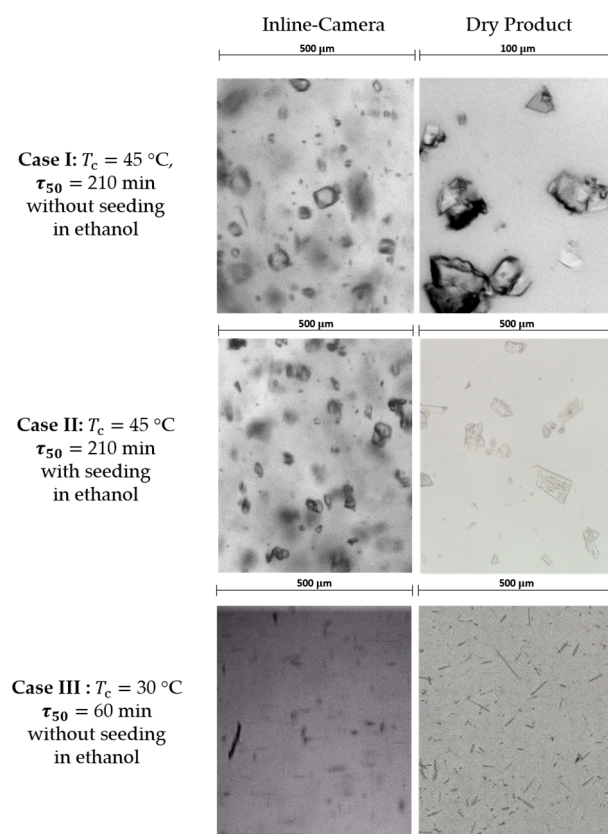


Figure 6. Images acquired by Crystalline (inline camera) and after drying (offline microscopic) for the crystal morphology analysis of the three cases to be validated in the I scale from Table 2.

The two scenarios (inline camera, offline/dry product) were assessed using a volumetric cumulative distribution, necessitating the transformation of their two-dimensional projections into a three-dimensional representation. To facilitate this transformation, we assumed an orthorhombic shape of the crystals, where the crystal depth is equal to the width of the crystals.

Figure 7 reveals a strong agreement in the morphologies measured inline and offline, particularly in Case I and Case II, where the aspect ratio tends towards unity. The *AR* shows minimal change after drying and shifts even more to 1. In Case I and Case II, the isometric crystals may mature and become even more isometric, or some of the needle-shaped crystals may break, contributing to more equant-shaped crystals. Regarding the crystal dimensions, Case II exhibited a significant increase of the median size, with a 50% length enlargement and a 70% width broadening, which likely contributed to the improved aspect ratio observed offline. Case I also showed a noteworthy 25% enlargement along x_{\max} and 33% along x_{\min} . This uneven enlargement, now higher along x_{\min} , further explains the observed trend towards a more isometric ratio after drying in the offline evaluation.

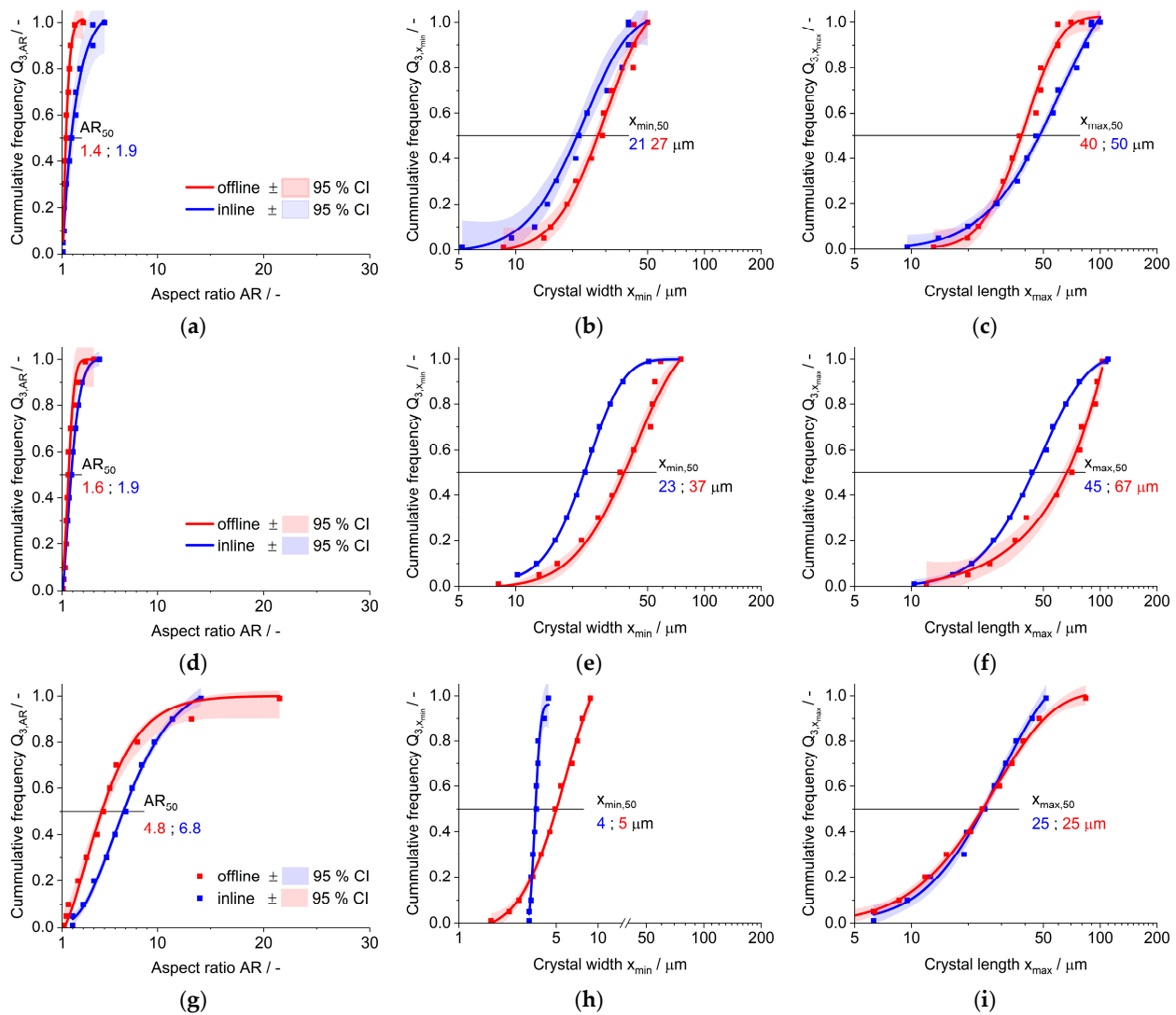


Figure 7. Cumulative distribution of aspect ratio (AR), crystal width (x_{\min}), and length (x_{\max}) for the cases shown in Figure 6. Data were obtained from the inline camera and offline images of the dry product. Case I (a–c), Case II (d–f), and Case III (g–i). Scale in (h) is interrupted between 10 and 50 for a better visualization.

The evaluation of Case III immediately reflects the already observed elongated aspect of the crystal on the microscopic images. The median length observed by the inline camera is at least five times longer than the median width. Secondly, the needle crystals are much smaller than the other cases. Thus, in this case, not only are the undesired acicular crystals produced but also much finer ones. The differences in the aspect ratio might not be only due to the reasons discussed above but may also stem from the extremely small width of the crystals, which challenge the minimal resolution of the inline camera. On the other hand, under the microscope used for the offline evaluation, a better resolution is achieved. This might explain the broader distribution of the cumulative frequency of x_{\min} in comparison with the inline curve.

In summary, the chosen cases clearly define specific goals for replicating crystal morphology on a larger scale. The crystal morphology remains consistent even after drying, with only a noticeable size increase. The increase in crystal size is a common and expected outcome during crystal product processing, highlighting the need to consider the entire process when assessing the final crystal morphology and size distribution [58–60].

3.2. Process Resemblancy

Variables such as the solvent and temperature can be transferred to larger scales without significant challenges. However, at the l scale, it is essential to make a precise adjustment of the fluid jacket temperature to achieve the desired evaporation rate, ensuring an equivalent supersaturation buildup comparable to that observed at the ml scale. All of the variables to set similar process conditions in both setups are listed in Table 3.

Table 3. Process conditions of the crystallization experiments at the ml scale and their counterpart at the l scale. Ethanol is used as the solvent in all experiments.

ml Scale									
Case	T_c °C	\dot{V}_{N_2} mL min ⁻¹	τ_{50} min	p mbar	$M_{Bit,seed}$ g	$S_{0,X}$ -	$V_{EtOH,0}$ mL	$M_{API,0}$ g	n min ⁻¹
I	45	37	210	970	0	1.45	5	0.952	1000
II	45	37	210	970	0.004	1.33	5	0.874	1000
III	30	220	60	970	0	1.49	5	0.333	1000
l Scale									
Case	T_c °C	T_H °C	τ_{50} min	p mbar	$M_{Bit,seed}$ g	$S_{0,X}$ -	$V_{EtOH,0}$ mL	$M_{API,0}$ g	n min ⁻¹
I-L	45	58	210	232	-	1.45	1090	207	178
II-L	45	58	210	232	0.425	1.37	1100	198	178
III-L	30	56	60	106	-	1.47	1200	72	178

Figure 8a–c presents the supersaturation buildup at the l scale, along with the trajectory from the ml scale. After nucleation, the supersaturation becomes nominal, serving primarily to visualize the similar evaporation time in both scales. Additionally, with the larger l scale setup, the increased size of the crystallizator allows us to take samples at various stages of the process. Using a density–mass fraction correlation, we can then calculate, offline, the Bitopertin mass fraction in the solution at specific time points, enabling us to determine the corresponding supersaturation ratios.

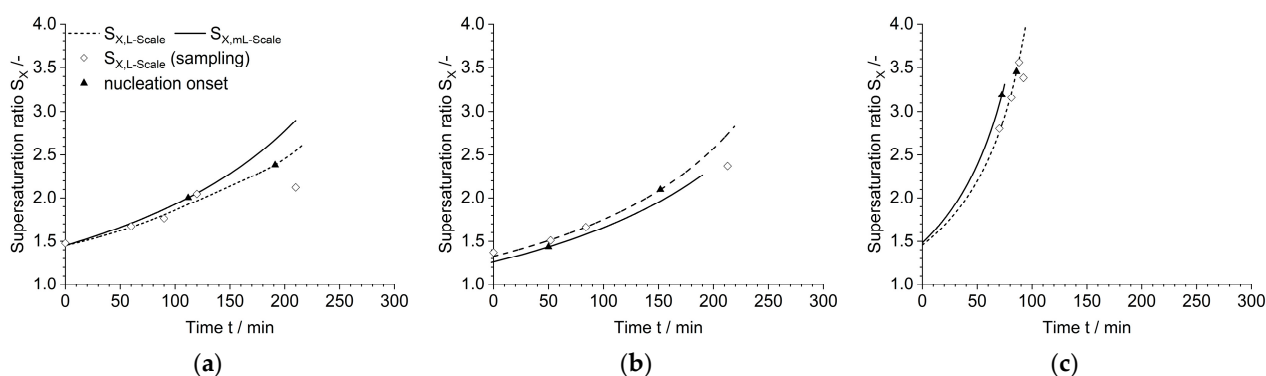


Figure 8. Comparison of the supersaturation buildup for the ml and l scales of Table 3. Case I and Case I-L (a), Case II and Case II-L (b), and Case III and Case III-L (c).

Overall, the supersaturation buildup succeeded under very similar conditions at both scales. Although the initial supersaturation at the l scale might vary slightly from the ml scale, the evaporation process proceeds at the same speed in both cases. On the other hand, significant differences were observed in the supersaturation levels at the moments of nucleation onset, which is not a rare phenomenon, as evidenced in various studies dealing with different volume scales [48,49,61–64]. Steendam et al. observed significantly higher nucleation rates for Paracetamol in a 10 mL volume compared with a 680 mL volume [48]. This observation suggests that, under identical conditions to those in the

10 mL volume, spontaneous nucleation at the 680 mL volume is more likely to occur at higher supersaturation levels. This difference on the nucleation onset must be carefully considered during crystal morphology analysis. For instance, in Case I-L, nucleation occurred at a higher supersaturation ratio compared with the corresponding mL scale case. Consequently, if the impact of supersaturation on triggering different crystal growth along the faces and tip of the crystal is substantial, more elongated crystals should be expected in Case I-L.

In Case II and Case II-L, the supersaturation begins to be depleted directly after seeding. However, before the onset of secondary nucleation, the mass of solids is significantly smaller in comparison with the total mass of Bitopertin in the solution. This explains why the supersaturation, measured by sampling, is in good agreement with the nominal supersaturation during a large interval. A surprising observation of Case II-L is the very delayed onset of secondary nucleation at the larger scale. Possible explanations align with the discussed points for Case I-L; there might be a generally smoother attrition in the L scale due to the larger available volume and less intense contact of the crystals with other crystals, walls, and other pieces in the crystallizer [48,53,64,65].

Lastly, in Case III and Case III-L, both display extremely late nucleation at 30 °C, and their supersaturation over time exhibits good agreement. Consequently, a very similar crystal morphology is expected. However, in these experiments, there is a slightly higher nucleation onset in the L scale, which may result in more elongated crystals in the L scale.

3.3. Large Crystallizer (L Scale)

The morphologies observed at the L scale demonstrate a strong resemblance to the results obtained at the mL scale. As depicted in Figure 9, it is evident that the morphology in Case I-L and Case II-L exhibits a trend towards more isometric shapes, unlike those observed in Case III-L, which, as aimed and anticipated, are clearly elongated.

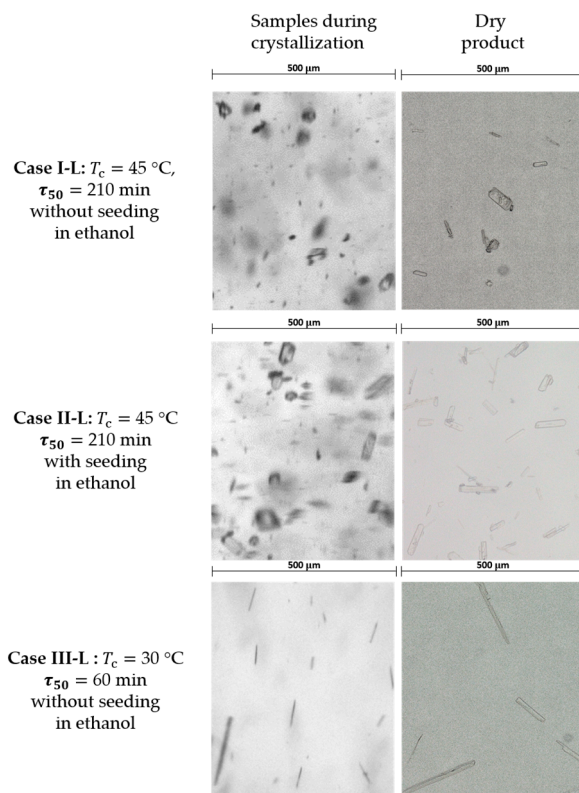


Figure 9. Images acquired by suspension sampling during the crystallization observed in Crystalline and after drying (offline) for the crystal morphology analysis of the three selected cases to be validated at the L scale.

Although the overall morphology remained visually similar, the quantitative evaluation presented in Figure 10 highlights the significant impact of the filtration and drying steps.

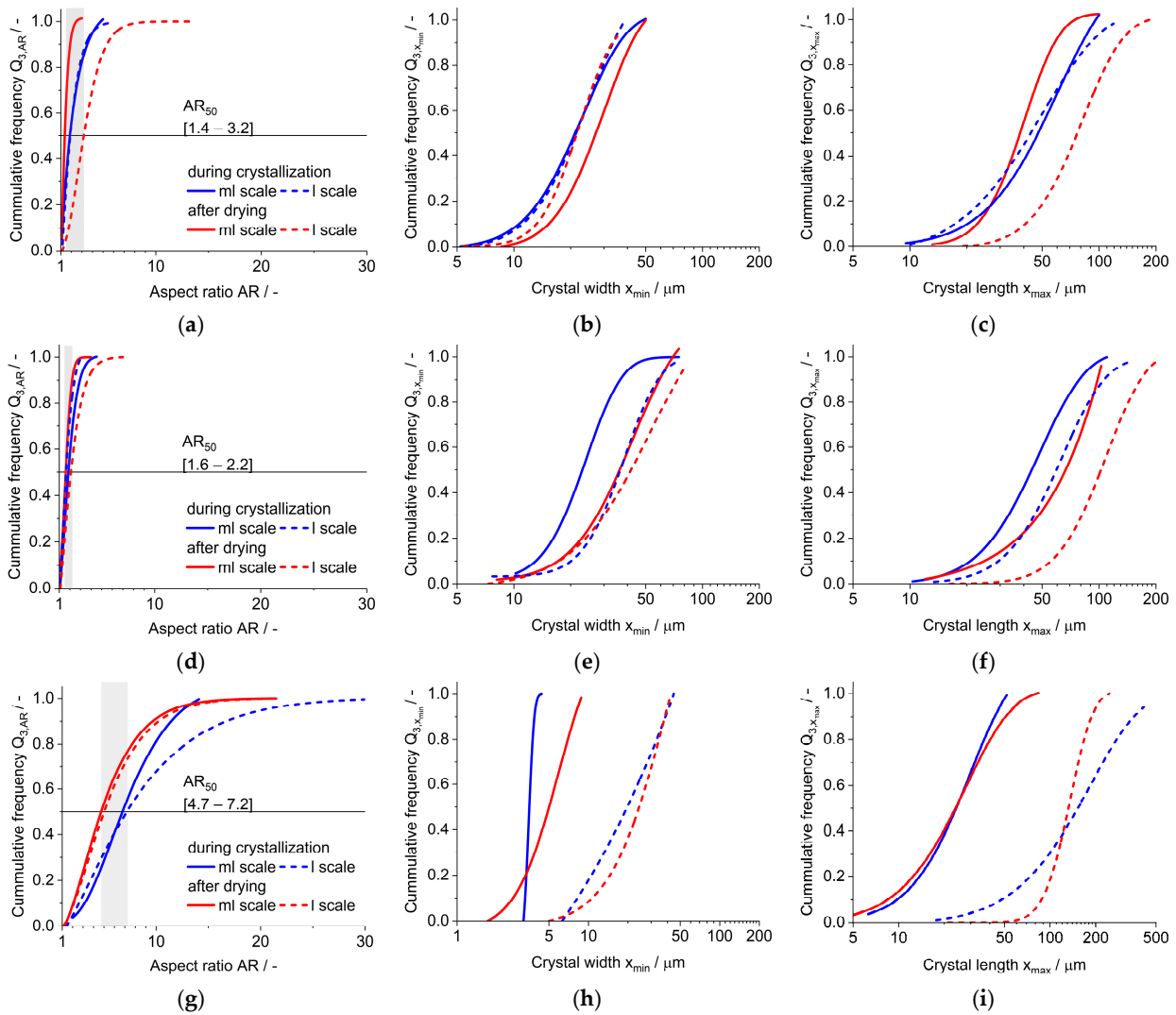


Figure 10. Comparison of the cumulative distribution of aspect ratio (AR), crystal width (x_{\min}) and length (x_{\max}), for the cases shown in Figures 6 and 9. Data obtained from inline images (ml scale) or samples during the crystallization (I scale) and after drying (both scales). Case I and I-L (a–c), Case II and II-L (d–f), and Case III and III-L (g–i). The gray area illustrates the range limits of the aspect ratio (AR) across the four cases.

Case II-L, which was also aimed at producing isometric crystals, showed a more favorable outcome. The variation in morphology, as assessed by the aspect ratio in Figure 10d, was significantly smaller compared with the previous case. Once again, the aspect ratio derived from the image analysis of the crystals in the suspension, both at the ml scale and during the process in the I scale, showed a closer similarity as the ones after drying. The only noticeable difference in the inline evaluation is the larger size of the crystals in the I scale setup. This might be attributed to less intense agitation, as also suggested by the delayed onset of secondary nucleation. In a similar manner as at the ml scale, at the I scale the filtration step posed a challenge that led to uneven crystal growth, resulting in greater elongation along x_{\max} compared with x_{\min} , as depicted in Figure 10e,f.

In the analysis of Case I-L, it is evident that the sample that was taken and analyzed during the crystallization exhibited almost identical aspect ratio, length, and width as

observed inline in the miniaturized scale. The slightly higher supersaturation onset did not seem to significantly elongate the crystals of Case I-L. However, after filtration and drying, the crystals experienced significant elongation, as shown in Figure 10b, with over 100% increase in $x_{\max,50}$. Although the aspect ratio (see Figure 10a) still falls within an acceptable range, it is not as isometric as observed at the miniaturized ml scale. The elongation along x_{\max} can be attributed to poor filtration, resulting in rapid evaporation of the mother liquor and promoting acicular growth.

In contrast with the previous cases, Case III-L focused on the crystallization of more acicular crystals. The aspect ratio analysis, depicted in Figure 10g, revealed that the morphology of the crystals remained very similar between the samples analyzed during the crystallization and after the solid–liquid separation. However, the most notable difference compared with the crystals obtained at the ml scale is the larger size of the crystals at the l scale, as can be noticed on Figure 10h,i. For instance, if $x_{\max,50}$ at the ml scale is 24.5 μm , its counterpart at the l scale reaches up to 102.3 μm . This suggests that the larger volume at the l scale crystallizer reduces the likelihood of crystal breakage compared with the ml scale. Interestingly, the comparison of results before and after solid–liquid separation showed a positive effect of filtration on the crystal morphology in both scales. The aspect ratio distribution shifted towards lower values, which we attribute to the high fragility of the elongated crystals and the easy breakage that occurs during the separation process.

3.4. Crystal Structure

Variations in morphology due to the presence of different polymorphs were dismissed by examining the X-ray diffractograms of the dried product. In all cases, the peaks matched those expected for polymorph A and did not reveal any additional peaks associated with other Bitopertin polymorphs. In Figure 11, X-ray diffractograms of needle and isometric crystals from Cases I-L and Case III-L are presented as exemplary illustrations. Notably, comparable patterns are observed in both cases, exhibiting a high correlation with the desired stable polymorph. The results remain consistent for the additional cases explored.

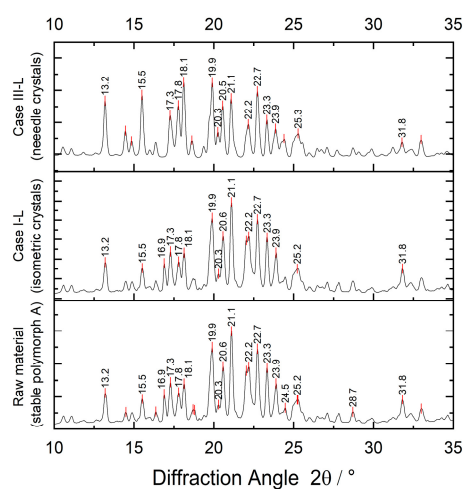


Figure 11. Diffractograms of needle and isometric crystals from Case I-L and Case III-L, respectively, compared with the reference material (stable polymorph A).

4. Discussion

Our results confirm the hypothesis that maintaining fidelity to the process conditions used in the ml scale experiments and ensuring a high level of resemblance between the scales in terms of geometry and operation conditions increases the likelihood of obtaining similar crystal morphologies. This result is of tremendous importance because the morphologies that result from screening experiments in miniaturized devices can be reproduced with a high degree of confidence by larger scale experiments.

Less satisfactory was the agreement regarding crystal size. However, as discussed above, a considerable variability on the nucleation kinetics is expected, affecting the resulting crystal size. A second explanation can be found in the different resulting agitation regime, even after our effort trying to resemble both. As can be seen in the comparisons of Case II (fast evaporation, seeded, 45 °C) and Case III (without seeding, fast evaporation, 30 °C) with their respective cases in l scales, there is a first hint in this direction based on the later onset of the nucleation at the l scale and a second hint with a noticeable shift to larger crystals, likely due to less attrition and crystal breakage. As pointed out before, the agitation conditions in the larger volume seem to be smoother in the triggering of shear between crystals with the walls, stirrer and other crystals as the ones ruling the miniaturized crystallizer. This highlights the need for more detailed analysis of the agitation by simulation programs. Although this aspect was omitted in the current study, it is believed that such an analysis could prove valuable in subsequent scaling-up steps. From an empirical point of view, a systematic study of the effect of agitation on the resulting crystal size may also improve this property. This is corroborated by findings in the foundational literature [66,67] and has been reinforced by recent studies [49,65] that demonstrate how the agitation can be employed as a control variable to reach desired crystal sizes. This is a property that holds significant importance in both the processability and formulation of the final product and is thereby influential on the therapeutic performance [14,24,68,69].

Furthermore, despite the general resemblance in morphology, the quantitative evaluation highlighted the significant influence of the filtration and drying steps on the crystal morphology. It is worth noting that the impact of these steps cannot be conclusively characterized as either positive or negative, as both elongation and reduction in the aspect ratio were observed. More importantly, from these observations derives the relevancy of the inline image analysis and the subsequent analysis after filtration and drying. These provide valuable insights into the effect of process conditions on the crystal morphology. Comparing the aspect ratio and crystal size curves obtained during crystallization, a higher degree of similarity is observed between the scales. However, after solid–liquid separation, the differences between the scales become more pronounced. These observations underscore the usefulness of inline imaging or analysis during crystallization. In Case I-L (without seeding, slow evaporation, 45 °C), where a more elongated aspect ratio is observed, improvements could potentially be achieved by adjusting the filtration procedure rather than the crystallization process, as the inline analysis reveals a good isometric morphology.

In summary, we successfully validated the morphologies observed in the small-scale (ml scale) experiments when scaled up by a factor of 200. This validation was the result of meticulous replication of the crystallization conditions. However, the comprehensive analysis also shed light on differences in crystal size, accentuated after filtration and drying, as has also been observed in [58–60]. Therefore, it becomes evident that the crystallization process alone may not always be the critical factor when obtaining a desired morphology. Other aspects, such as poor filtration or drying processes, can also play a crucial role. Hence, it is essential to thoroughly review and consider these factors before making decisions aimed at achieving the desired crystal morphology in larger-scale production.

5. Conclusions

Our investigation validates the transferability of crystal morphologies from ml scale experiments to l scale, by a factor of 200. While successful in maintaining overall morphology, variations in crystal size expose expected intricacies influenced by spontaneous nucleation and agitation regimes that are not entirely equivalent. This insight becomes crucial for future scaling-up steps, where meticulous control over these aspects could potentially enhance reproducibility in terms of crystal size.

Moreover, the study unveils the significant impact of filtration and drying processes on crystal size and morphology. The multifaceted influence of these steps, evident in variations in post-solid–liquid separation, prompts a comprehensive consideration of their role in achieving desired outcomes at larger scales. The findings stress the importance

of not only scrutinizing the crystallization process but also thoroughly evaluating downstream processes.

Finally, this study contributes valuable insights to the field, providing more certainties that experiments from miniaturized crystallizers are in large extent consistent with the outcomes or larger scales.

Author Contributions: Conceptualization, N.A.R.O. and M.K.; methodology, N.A.R.O.; software, N.A.R.O.; validation, N.A.R.O.; formal analysis, N.A.R.O. and M.K.; investigation, N.A.R.O.; data curation, N.A.R.O.; writing—original draft preparation, N.A.R.O.; writing—review and editing, N.A.R.O. and M.K.; visualization, N.A.R.O.; supervision, M.K.; project administration, M.K.; funding acquisition, M.K. All authors have read and agreed to the published version of the manuscript.

Funding: This research was funded by F. Hoffmann-La Roche within the framework of the project EPBA2261991-A17.

Data Availability Statement: Data are contained within the article. The data and methods used in the research are presented in sufficient detail in the document for other researchers to replicate the work.

Acknowledgments: The authors sincerely thank Ralph Diodone and Pirmin Hidber from F. Hoffmann-La Roche for their invaluable feedback and contributions throughout this research project. Their expertise has greatly influenced the direction and quality of our study. We acknowledge support by the KIT-Publication Fund of the Karlsruhe Institute of Technology.

Conflicts of Interest: The authors declare no conflict of interest. The funders had no role in the design of the study; in the collection, analyses, or interpretation of data; or in the writing of the manuscript. The funders retain their legal right to make the decision regarding the publication of the results.

References

1. Dandekar, P.; Kuvadia, Z.B.; Doherty, M.F. Engineering Crystal Morphology. *Annu. Rev. Mater. Res.* **2013**, *43*, 359–386. [[CrossRef](#)]
2. Lovette, M.A.; Browning, A.R.; Griffin, D.W.; Sizemore, J.P.; Snyder, R.C.; Doherty, M.F. Crystal Shape Engineering. *Ind. Eng. Chem. Res.* **2008**, *47*, 9812–9833. [[CrossRef](#)]
3. Pu, S.; Hadinoto, K. Habit Modification in Pharmaceutical Crystallization: A Review. *Chem. Eng. Res. Des.* **2024**, *201*, 45–66. [[CrossRef](#)]
4. Pudasaini, N.; Upadhyay, P.P.; Parker, C.R.; Hagen, S.U.; Bond, A.D.; Rantanen, J. Downstream Processability of Crystal Habit-Modified Active Pharmaceutical Ingredient. *Org. Process Res. Dev.* **2017**, *21*, 571–577. [[CrossRef](#)]
5. Bourcier, D.; Féraud, J.P.; Colson, D.; Mandrick, K.; Ode, D.; Brackx, E.; Puel, F. Influence of Particle Size and Shape Properties on Cake Resistance and Compressibility during Pressure Filtration. *Chem. Eng. Sci.* **2016**, *144*, 176–187. [[CrossRef](#)]
6. Datir, S.R.; Kumar, D.; Bele, M.H. Modified Crystal Habits of Glimepiride to Improve Manufacturing Processability. *J. Cryst. Growth* **2022**, *592*, 126711. [[CrossRef](#)]
7. Mirza, S.; Miroshnyk, I.; Heinämäki, J.; Antikainen, O.; Rantanen, J.; Vuorela, P.; Vuorela, H.; Yliruusi, J. Crystal Morphology Engineering of Pharmaceutical Solids: Tableting Performance Enhancement. *AAPS PharmSciTech* **2009**, *10*, 113–119. [[CrossRef](#)]
8. Tiwary, A.K. Modification of Crystal Habit and Its Role in Dosage Form Performance. *Drug Dev. Ind. Pharm.* **2001**, *27*, 699–709. [[CrossRef](#)]
9. Blagden, N.; Matas, M.; Gavan, P.T.; York, P. Crystal Engineering of Active Pharmaceutical Ingredients to Improve Solubility and Dissolution Rates. *Adv. Drug Deliv. Rev.* **2007**, *59*, 617–630. [[CrossRef](#)]
10. Phan, C.U.; Shen, J.; Yu, K.; Mao, J.; Tang, G. Impact of Crystal Habit on the Dissolution Rate and In Vivo Pharmacokinetics of Sorafenib Tosylate. *Molecules* **2021**, *26*, 3469. [[CrossRef](#)]
11. Modi, S.R.; Dantuluri, A.K.R.; Perumalla, S.R.; Sun, C.C.; Bansal, A.K. Effect of Crystal Habit on Intrinsic Dissolution Behavior of Celecoxib Due to Differential Wettability. *Cryst. Growth Des.* **2014**, *14*, 5283–5292. [[CrossRef](#)]
12. Dali, M.V.; Carstensen, J.T. Effect of Change in Shape Factor of a Single Crystal on Its Dissolution Behavior. *Pharm. Res.* **1996**, *13*, 155–162. [[CrossRef](#)] [[PubMed](#)]
13. Ren, Y.; Shen, J.; Yu, K.; Phan, C.U.; Chen, G.; Liu, J.; Hu, X.; Feng, J. Impact of Crystal Habit on Solubility of Ticagrelor. *Crystals* **2019**, *9*, 556. [[CrossRef](#)]
14. Cote, A.; Erdemir, D.; Girard, K.P.; Green, D.A.; Lovette, M.A.; Sirota, E.; Nere, N.K. Perspectives on the Current State, Challenges, and Opportunities in Pharmaceutical Crystallization Process Development. *Cryst. Growth Des.* **2020**, *20*, 7568–7581. [[CrossRef](#)]
15. Bötschi, S.; Rajagopalan, A.K.; Rombaut, I.; Morari, M.; Mazzotti, M. From Needle-like toward Equant Particles: A Controlled Crystal Shape Engineering Pathway. *Comput. Chem. Eng.* **2019**, *131*, 106581. [[CrossRef](#)]
16. Civati, F.; O'Malley, C.; Erxleben, A.; McArdle, P. Factors Controlling Persistent Needle Crystal Growth: The Importance of Dominant One-Dimensional Secondary Bonding, Stacked Structures, and van Der Waals Contact. *Cryst. Growth Des.* **2021**, *21*, 3449–3460. [[CrossRef](#)] [[PubMed](#)]

17. Lovette, M.A.; Doherty, M.F. Needle-Shaped Crystals: Causality and Solvent Selection Guidance Based on Periodic Bond Chains. *Cryst. Growth Des.* **2013**, *13*, 3341–3352. [[CrossRef](#)]
18. Wells, A.F. XXV. Crystal Habit and Internal Structure.—II. *Lond. Edinb. Dublin Philos. Mag. J. Sci.* **1946**, *37*, 217–236. [[CrossRef](#)]
19. Klapwijk, A.R.; Simone, E.; Nagy, Z.K.; Wilson, C.C. Tuning Crystal Morphology of Succinic Acid Using a Polymer Additive. *Cryst. Growth Des.* **2016**, *16*, 4349–4359. [[CrossRef](#)]
20. Croker, D.M.; Kelly, D.M.; Horgan, D.E.; Hodnett, B.K.; Lawrence, S.E.; Moynihan, H.A.; Rasmuson, Å.C. Demonstrating the Influence of Solvent Choice and Crystallization Conditions on Phenacetin Crystal Habit and Particle Size Distribution. *Org. Process Res. Dev.* **2015**, *19*, 1826–1836. [[CrossRef](#)]
21. Burton, W.K.; Cabrera, N.T.; Frank, F.C. The Growth of Crystals and the Equilibrium Structure of Their Surfaces. *Trans. R. Soc. Lond. Ser. A* **1951**, *244*, 299–358.
22. Fischer, C.; Drummer, D. Crystallization and Mechanical Properties of Polypropylene under Processing-Relevant Cooling Conditions with Respect to Isothermal Holding Time. *Int. J. Polym. Sci.* **2016**, *2016*, 5450708. [[CrossRef](#)]
23. Prywer, J. Kinetic and Geometric Determination of the Growth Morphology of Bulk Crystals: Recent Developments. *Prog. Cryst. Growth Charact. Mater.* **2005**, *50*, 1–38. [[CrossRef](#)]
24. Shekunov, B.Y.; York, P. Crystallization Processes in Pharmaceutical Technology and Drug Delivery Design. *J. Cryst. Growth* **2000**, *211*, 122–136. [[CrossRef](#)]
25. Said, A.; Louhi-Kultanen, M. Simulation and Empirical Studies of Solvent Evaporation Rates in Vacuum Evaporation Crystallization. *Chem. Eng. Technol.* **2019**, *42*, 1452–1457. [[CrossRef](#)]
26. Liang, Z.; Zhang, M.; Wu, F.; Chen, J.-F.; Xue, C.; Zhao, H. Supersaturation Controlled Morphology and Aspect Ratio Changes of Benzoic Acid Crystals. *Comput. Chem. Eng.* **2017**, *99*, 296–303. [[CrossRef](#)]
27. Wang, C.; Zhang, X.; Du, W.; Huang, Y.; Guo, M.; Li, Y.; Zhang, Z.; Hou, B.; Yin, Q. Effects of Solvent and Supersaturation on Crystal Morphology of Cefaclor Dihydrate: A Combined Experimental and Computer Simulation Study. *CrystEngComm* **2016**, *18*, 9085–9094. [[CrossRef](#)]
28. Takiyama, H. Supersaturation Operation for Quality Control of Crystalline Particles in Solution Crystallization. *Adv. Powder Technol.* **2012**, *23*, 273–278. [[CrossRef](#)]
29. Boerrigter, S.X.M.; Cuppen, H.M.; Ristic, R.I.; Sherwood, J.N.; Bennema, P.; Meekes, H. Explanation for the Supersaturation-Dependent Morphology of Monoclinic Paracetamol. *Cryst. Growth Des.* **2002**, *2*, 357–361. [[CrossRef](#)]
30. Li, J.; Doherty, M.F. Steady State Morphologies of Paracetamol Crystal from Different Solvents. *Cryst. Growth Des.* **2017**, *17*, 659–670. [[CrossRef](#)]
31. Davey, R.J. The Role of the Solvent in Crystal Growth from Solution. *J. Cryst. Growth* **1986**, *76*, 637–644. [[CrossRef](#)]
32. Horst, J.H.; Geertman, R.M.; van Rosmalen, G.M. The Effect of Solvent on Crystal Morphology. *J. Cryst. Growth* **2001**, *230*, 277–284. [[CrossRef](#)]
33. Stoica, C.; Verwer, P.; Meekes, H.; van Hoof, P.J.C.M.; Kaspersen, F.M.; Vlieg, E. Understanding the Effect of a Solvent on the Crystal Habit. *Cryst. Growth Des.* **2004**, *4*, 765–768. [[CrossRef](#)]
34. Soper, E.M.; Penchev, R.Y.; Todd, S.M.; Eckert, F.; Meunier, M. Quantifying the Effect of Solvent on the Morphology of Organic Crystals Using a Statistical Thermodynamics Approach. *J. Cryst. Growth* **2022**, *591*, 126712. [[CrossRef](#)]
35. Ji, X.; Wang, J.; Wang, T.; Huang, X.; Li, X.; Wang, N.; Huang, Y.; Li, R.; Zhao, B.; Zhang, T.; et al. Understanding the Role of Solvent in Regulating the Crystal Habit. *CrystEngComm* **2022**, *24*, 2226–2240. [[CrossRef](#)]
36. Zhu, D.; Zhang, S.; Cui, P.; Wang, C.; Dai, J.; Zhou, L.; Huang, Y.; Hou, B.; Hao, H.; Zhou, L.; et al. Solvent Effects on Catechol Crystal Habits and Aspect Ratios: A Combination of Experiments and Molecular Dynamics Simulation Study. *Crystals* **2020**, *10*, 316. [[CrossRef](#)]
37. Turner, T.D.; Hatcher, L.E.; Wilson, C.C.; Roberts, K.J. Habit Modification of the Active Pharmaceutical Ingredient Lovastatin Through a Predictive Solvent Selection Approach. *J. Pharm. Sci.* **2019**, *108*, 1779–1787. [[CrossRef](#)]
38. Wang, Y.; Liang, Z. Solvent Effects on the Crystal Growth Structure and Morphology of the Pharmaceutical Dirithromycin. *J. Cryst. Growth* **2017**, *480*, 18–27. [[CrossRef](#)]
39. Wilkinson, M.R.; Martinez-Hernandez, U.; Huggon, L.K.; Wilson, C.C.; Castro Dominguez, B. Predicting Pharmaceutical Crystal Morphology Using Artificial Intelligence. *CrystEngComm* **2022**, *24*, 7545–7553. [[CrossRef](#)]
40. Achermann, R.; Adams, R.; Prasser, H.-M.; Mazzotti, M. Characterization of a Small-Scale Crystallizer Using CFD Simulations and X-ray CT Measurements. *Chem. Eng. Sci.* **2022**, *256*, 117697. [[CrossRef](#)]
41. Simone, E.; McVeigh, J.; Reis, N.M.; Nagy, Z.K. A High-Throughput Multi-Microfluidic Crystal Generator (MMicroCryGen) Platform for Facile Screening of Polymorphism and Crystal Morphology for Pharmaceutical Compounds. *Lab Chip* **2018**, *18*, 2235–2245. [[CrossRef](#)] [[PubMed](#)]
42. Jain, D.; Dalvi, V.; Mathpati, C.; Kant, J. Process Analytical Technology as an Enabling Tool for Scale up of Crystallization, Filtration, Drying and Milling. *Chem. Eng. Res. Des.* **2023**, *190*, 117–128. [[CrossRef](#)]
43. Nguyen, T.T.H.; Turner, T.D.; Matinong, A.M.E.; Marziano, I.; Hammond, R.B.; Roberts, K.J. Measured Growth Rates of Ibuprofen: Comparing Single Crystal and Bulk Suspensions Data. *Chem. Eng. Technol.* **2021**, *44*, 1287–1293. [[CrossRef](#)]
44. Barros Groß, M.; Kind, M. From Microscale Phase Screening to Bulk Evaporative Crystallization of Proteins. *J. Cryst. Growth* **2018**, *498*, 160–169. [[CrossRef](#)]

45. Yi, Y.J.; Myerson, A.S. Laboratory Scale Batch Crystallization and the Role of Vessel Size. *Chem. Eng. Res. Des.* **2006**, *84*, 721–728. [[CrossRef](#)]
46. Kramer, H.J.M.; Bermingham, S.K.; van Rosmalen, G.M. Design of Industrial Crystallisers for a given Product Quality. *J. Cryst. Growth* **1999**, *198*, 729–737. [[CrossRef](#)]
47. Feth, M.P.; Heyse, W.; Baumgartner, B.; Nagel, N.; Tappertzhofen, C.; Olpp, T.; Jurascheck, J.; Ulrich, J.; Helmdach, L.; Petzoldt, C. From Laboratory to Pilot Plant: The Solid-State Process Development of a Highly Potent Cathepsin S/K Inhibitor. *Eur. J. Pharm. Biopharm.* **2013**, *83*, 436–448. [[CrossRef](#)]
48. Steendam, R.R.E.; Keshavarz, L.; Blijlevens, M.A.R.; Souza, B.; Croker, D.M.; Frawley, P.J. Effects of Scale-Up on the Mechanism and Kinetics of Crystal Nucleation. *Cryst. Growth Des.* **2018**, *18*, 5547–5555. [[CrossRef](#)]
49. Yu, Z.-Q.; Yeoh, A.; Chow, P.S.; Tan, R.B.H. Particle Size Control in Batch Crystallization of Pyrazinamide on Different Scales. *Org. Process Res. Dev.* **2016**, *20*, 2100–2107. [[CrossRef](#)]
50. Smejkal, B.; Helk, B.; Rondeau, J.-M.; Anton, S.; Wilke, A.; Scheyerer, P.; Fries, J.; Hekmat, D.; Weuster-Botz, D. Protein Crystallization in Stirred Systems—Scale-up via the Maximum Local Energy Dissipation. *Biotechnol. Bioeng.* **2013**, *110*, 1956–1963. [[CrossRef](#)]
51. Ramos Ojeda, N.; Kind, M. A Comprehensive Workflow Towards More Equant Shaped Crystals of Active Pharmaceutical Ingredients. *Chem. Eng. Technol.* **2023**, *43*, 1–12. [[CrossRef](#)]
52. Bubendorf, A.; Deynet-Vucenovic, A.; Diodone, R.; Grassmann, O.; Lindenstruth, K.; Pinard, E.; Rohrer, F.E.; Schwitter, U. Hoffmann-La Roche INC. Solid Forms of 4-(3-Fluoro-5-Trifluoromethyl Pyridin-2-Yl)-Piperazin-1-Yl-5-Methanesulfonyl-2-(S)-2,2,2-Trifluoro-1-Methyl-Ethoxy)-Phenyl-Methanone. U.S. Patent US2008/0214561A1, 4 September 2008.
53. Qian, R.Y.; Chen, Z.D.; Ni, H.G.; Fan, Z.Z.; Cai, F.D. Crystallization Kinetics of Potassium Chloride from Brine and Scale-up Criterion. *AIChE J.* **1987**, *33*, 1690–1697. [[CrossRef](#)]
54. Henzler, H.J.; Biedermann, A. Modelluntersuchungen Zur Partikelbeanspruchung in Reaktoren. *Chem. Ing. Tech.* **1996**, *68*, 1546–1561. [[CrossRef](#)]
55. Hebel, D.; Ürdingen, M.; Hekmat, D.; Weuster-Botz, D. Development and Scale up of High-Yield Crystallization Processes of Lysozyme and Lipase Using Additives. *Cryst. Growth Des.* **2013**, *13*, 2499–2506. [[CrossRef](#)]
56. Lehrer, I.H. Jacket-Side Nusselt Number. *Ind. Eng. Chem. Process Des. Dev.* **1970**, *9*, 553–558. [[CrossRef](#)]
57. European Directorate for the Quality of Medicines & HealthCare. *European Pharmacopoeia*, 8th ed.; Council of Europe: Strasbourg, France, 2013.
58. Borho, K.; Polke, R.; Wintermatel, K.; Schubert, H.; Sommer, K. Produkteigenschaften und Verfahrenstechnik. *Chem. Ing. Tech.* **1991**, *63*, 792–808. [[CrossRef](#)]
59. Steenweg, C.; Habicht, J.; Wohlgemuth, K. Continuous Isolation of Particles with Varying Aspect Ratios up to Thin Needles Achieving Free-Flowing Products. *Crystals* **2022**, *12*, 137. [[CrossRef](#)]
60. Mahdi, F.M.; Shier, A.P.; Fragkopoulos, I.S.; Carr, J.; Gajjar, P.; Muller, F.L. On the Breakage of High Aspect Ratio Crystals in Filter Beds under Continuous Percolation. *Pharm. Res.* **2020**, *37*, 231. [[CrossRef](#)]
61. Selzer, D.R. *On Primary Crystal Nucleation in Electrolyte Solutions of Well-Soluble Substances Primary Nucleation Kinetics and Nucleation Mechanisms at Low and High Supersaturation*, Karlsruhe Institute für Technologie: Karlsruhe; Verlag Dr. Hut: München, Germany, 2021.
62. Devos, C.; van Gerven, T.; Kuhn, S. A Review of Experimental Methods for Nucleation Rate Determination in Large-Volume Batch and Microfluidic Crystallization. *Cryst. Growth Des.* **2021**, *21*, 2541–2565. [[CrossRef](#)]
63. Xiao, Y.; Wang, J.; Huang, X.; Shi, H.; Zhou, Y.; Zong, S.; Hao, H.; Bao, Y.; Yin, Q. Determination Methods for Crystal Nucleation Kinetics in Solutions. *Cryst. Growth Des.* **2018**, *18*, 540–551. [[CrossRef](#)]
64. Yokota, M.; Takezawa, E.; Takakusaki, T.; Sato, A.; Takahashi, H.; Kubota, N. Scale-up effect on the Rate of Contact Nucleation Caused by Collisions of Crystals with an Impeller. *Chem. Eng. Sci.* **1999**, *54*, 3831–3838. [[CrossRef](#)]
65. Li, X.; Heng, J.Y.Y. The Critical Role of Agitation in Moving from Preliminary Screening Results to Reproducible Batch Protein Crystallisation. *Chem. Eng. Res. Des.* **2021**, *173*, 81–88. [[CrossRef](#)]
66. Mullin, J.W. *Crystallization*; Chemical, Petrochemical & Process; Butterworth-Heinemann: Oxford, UK, 2001; ISBN 978-0-7506-4833-2.
67. Mersmann, A. (Ed.) *Crystallization Technology Handbook*; CRC Press: New York, NY, USA; Basel, Switzerland, 2001; ISBN 978-0-429-20798-3.
68. Rajagopalan, A.K.; Schneeberger, J.; Salvatori, F.; Bötschi, S.; Ochsenbein, D.R.; Oswald, M.R.; Pollefeys, M.; Mazzotti, M. A Comprehensive Shape Analysis Pipeline for Stereoscopic Measurements of Particulate Populations in Suspension. *Powder Technol.* **2017**, *321*, 479–493. [[CrossRef](#)]
69. Li, P.; He, G.; Lu, D.; Xu, X.; Chen, S.; Jiang, X. Crystal Size Distribution and Aspect Ratio Control for Rodlike Urea Crystal via Two-Dimensional Growth Evaluation. *Ind. Eng. Chem. Res.* **2017**, *56*, 2573–2581. [[CrossRef](#)]

Disclaimer/Publisher’s Note: The statements, opinions and data contained in all publications are solely those of the individual author(s) and contributor(s) and not of MDPI and/or the editor(s). MDPI and/or the editor(s) disclaim responsibility for any injury to people or property resulting from any ideas, methods, instructions or products referred to in the content.